PROBING HIGH ENERGY ELECTRON CALIBRATION WITH THE ATLAS DETECTOR

Summer Student Project Report

Student: Daliborka Hranjec (University of Kragujevac)

Supervisors: Martina Laura Ojeda (CERN), Stefano Manzoni (CERN)

August 2025

Abstract

Previous ATLAS detector energy calibration studies (e.g., [1] and [2]) were mainly concerned with the low-mid energy range ($p_{\mathrm{T}} < 300$ GeV), and the accuracy of the derived calibration on higher energies was not probed before. This project aims to inspect the existing calibration in said energy region, particularly looking into the effects of different electronic gains used by the ATLAS calorimeter detector, and examine potential ways for its improvement.

1 Introduction

The electron energy calibration for the ATLAS detector currently used for the high energy regions is the one based on the low to mid energy electrons, but due to nonlinearities in the energy response of the calorimeter, this result may not be optimal for the electrons of high energy. This analysis aims to inspect how well the existing calibration functions in the high energy region, which was not the focus of the previously published papers.

Section 2 gives an overview of ATLAS detector (Subsection 2.1) and its particle detection and reconstruction systems (Subsection 2.2). An overview of the calibration process (Subsection 2.3) and energy scale determination (Subsection 2.4) is also provided.

Section 3 explains details of the conducted study. It first describes the preliminary inspection of the sample statistics as well as the process of selecting the studied regions (Subsection 3.1). This is followed by the description of the fitting procedure performed to extract additional high energy scale corrections, concretely line-shape fit (Subsection 3.3).This is followed by the description of the fitting procedures performed to extract additional high energy scale corrections (Subsection 3.3), concretely two performed fits - line-shape fit (Subsection 3.3.1) and template fit (Subsection 3.3.2).

Section 4 then provides an overview of the different corrections obtained in this analysis, as well as the comparison with the results of the previous analyses and future outlooks.

2 Instrumentation and Theory Overview

2.1 ATLAS Detector

In this section an overview of ATLAS detector's regions is given, while more information can be found in [2] and in [3].

Radial segments surrounding the beampipe into which the ATLAS detector is divided can be seen on Figure 1 (Left) and are the following:

1. **Inner tracking detector (ID)** consisting of:
   - **pixel layer**
   - **silicon microstrip detector (SCT)**,
   - **transition radiation tracker (TRT)**.

   This segment enables measurement of primary and secondary vertices, as well as photon conversion vertices[1], reconstruction of the tracks and momenta of charged particles, as well as discrimination between different types of particles.

2. **Superconducting solenoids** - create magnetic field crucial for ID operation, in particular for the charged particle momentum measurement.

3. **Presampler layer (PS)** - enables correction for energy losses upstream of the calorimeter.

4. **Electromagnetic (EM) calorimeter** - enables precise measurement of energies of electrons and photons from collisions. It is divided into three regions:
   - a **barrel section (EMB)**: $|\eta| < 1.475$,
   - two **endcap sections (EMEC)**: $1.375 < |\eta| < 3.2$.

   The accordion geometry of its lead absorbers and electrodes provides a full coverage in ϕ. The absorbers are immersed in liquid-argon (LAr) as sampling medium. The EMB consists of three layers, while endcap has two layers with different number and size of cells, necessary for measuring the direction of the showers of the electromagnetically charged particles. Existence of multiple layers is also important for distinguishing between different particles. For example, electron showers deposit most of their energy on the second layer, and only smaller amounts of energy in third layer. Different granularity of the layer cells also has a role in particle identification. Converted photons identification, for example, benefits from the possibility of observing tracks of two electrons near each other in the first layer with high granularity. An illustration of the barrel layers is given on Figure 1 (Right).

[1] These vertices are produced when photon undergoes the process of electron-positron pair production

5. **Hadronic calorimeter** - enables precise measurement of energies of hadronic particles from collisions.

6. **Muon spectrometer** - located behind the calorimeters, enables accurate measurement for highly penetrative muons.

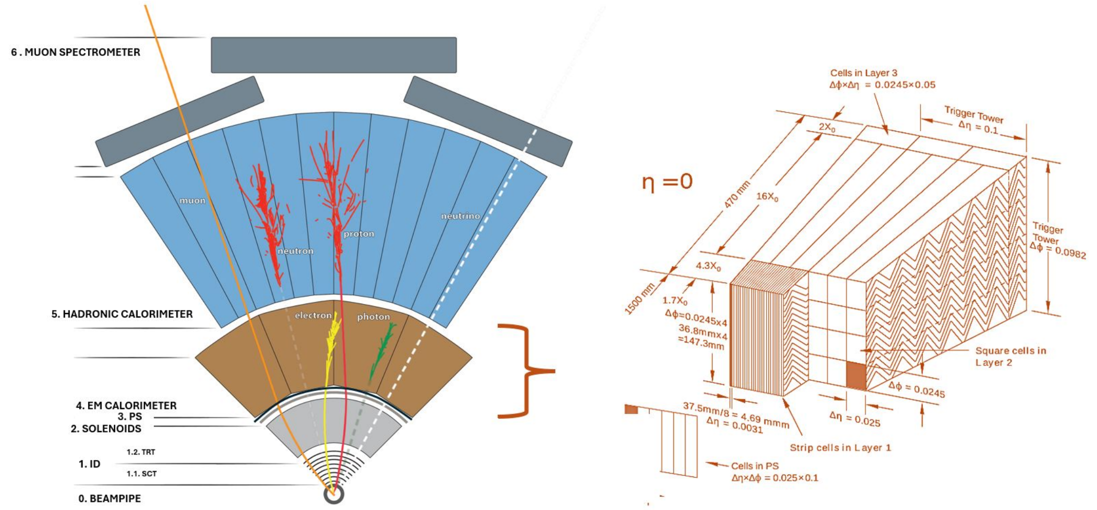

Figure 1: Left: Schematic overview of the ATLAS detector cross-section [4]; Right: Sketch of a barrel EM calorimeter module - adapted from [3].

2.2 Detection and reconstruction of electrons and photons

In this section a brief overview of the electron and photon detection and reconstruction process is given, while more details can be found in [2] and [5].

Electrons interact with the ID material, leaving a track, and their paths are curved in the magnetic field generated by solenoid magnets surrounding it. After passing through the ID electrons enter the EM calorimeter, in which they generate electromagnetic showers. Photons leave the track in the ID only if they undergo a process of pair-creation, i.e. if they are converted photons, and also create electromagnetic showers upon entering EM calorimeter. This serves as a way of discrimination between the two particles and also between the converted and unconverted photons, depending on the existence of the tracks and conversion vertices that can be associated with showers.

Ionizing particles from the showers created by electrons and photons produce a current within the electromagnetic calorimeter cell that is then collected, amplified, and shaped. The signal is sampled at $40MHz$ and digitized using the analog-to-digital converters (ADCs). Depending on the ADC counts, the signal is amplified using one of the three different gain modes:

- high-gain (HG) for particles with the lowest energy,
- medium-gain (MG),
- and low-gain (LG) for particles with the highest energy.

Electrons and photons are reconstructed from energy deposits in calorimeter cells using a variable cluster size algorithm. Eventual tracks in the ID are matched to the clusters in the EM calorimeter, and are used to define electrons and converted photons in the reconstruction process.

Although photons and electrons are different particles, with their own sets of properties, they can produce similar signatures in the detector. Electromagnetic showers produced by electrons can include photons from bremsstrahlung, while photon interactions include electrons created by the process of pair-production which leaves electron-like signatures. On the other hand, and more importantly, jets created by other particles in the detector can also, under some circumstances, be identified as electron showers. Different selection criteria are applied in order to minimize the number of misidentified particles, but with important tradeoff between purity of the sample and efficiency of the identification. For electrons there are four operating points: Very Loose, Loose, Medium and Tight.

2.3 Overview of the Calibration Procedure

Energy deposits measured during data runs usually do not perfectly represent the amount of energy that is actually being carried by the particles exiting a collision due to various imperfections of the detector. On the opposite side, generated simulations are made based on the best-known detector model, and are therefore deviating from the results obtained in a real detector. They can also account only for a part of processes that happen in an actual detector, but can never simulate every single one of them. This leads too a need to calibrate data so they better match what is actually happening in the experiment, and to calibrate the simulations so they better reflect the real-world conditions.

In the process of energy calibration several effects need to be accounted for in order to obtain the highly precise energy measurement, essential for all of the further analyses. The illustration of the process is given on the Figure 2, and the description below uses the same numbering to mark certain parts of the process. A more detailed account can be found in [1], [2] and [6].

1. As mentioned in Section 2.1, EM calorimeter is separated longitudinally into the layers with different characteristics. These layers need to be calibrated separately and then intercalibrated in order to equalize their energy scales.

2. This step includes a regression in which the true energy is extracted from the raw reconstructed energy. Simulations include a large variety of effects but can still differ from data by not including all of them, or being too optimistic in their predictions. It is therefore important to compare simulations to the real data, and from this comparison extract calibration constants, which are first applied to simulation samples and then also to data.

3. Additional corrections must be applied to account for the variations in the response of calorimeter cells in different detector regions (due to variations in the detector's electric field, gravitational bending of parts of the detector, etc.). It is also important to maintain overall detector's stability over time and different collision parameters.

   Another important step of the calibration is accounting for inherent nonlinearities related to the electronics readout system. When the signal from the cell is digitized calculations consider linear conversion from ADC counts to current and then from current to energy. In reality this process is intrinsically non-linear due to the characteristics of the electronics, which contributes to the nonlinearity of the electron and photon energy measurement. Since the said nonlinearity is dependent on the energy, it also makes direct comparison of the energy response in different readout gains complicated. Besides measuring nonlinearities and using them to linearize the response, it is also important to perform the intercalibration of the responses in the different gain modes (which is assumed to be perfect in the simulation, but is not in the real detector). Previous papers concerned more with intercalibration of the HG and MG, while the goal of this project was to investigate intercalibration of the MG and LG.

To finalize the calibration process, the $Z \to ee$ samples are used because this process is well understood and provides a clean signature, as well as high statistics. To make the ideal simulation response better match the actual detector data two more calibration steps are done.

4. The energy resolution is determined by observing that the width of the invariant mass peak for the electron pair from Z decay and is somewhat worse in the data than in the simulation. From this comparison smearing parameters can be extracted and then applied to the simulation data so it better matches the real data.

5. To account for the differences between data and simulation that are left after initial calibration the position of the electron pair invariant mass peak is compared in the simulation (where it ideally matches the Z mass) and in the data. Corrections are then applied so that peak positions in data match the Z mass. These corrections are not linear as the function of the electron energies, so they need to be separately set for different energies using the broad range of the Z-decay electrons.

Finally, additional calibration needs to be performed to account for photon-specific effects and ensure the accurate photon energy measurement.

6. Parts of photon shower energy are not deposited in the calorimeter, since they can extend both laterally, to the neighboring cells, and longitudinally, deeper into the calorimeter. Additional corrections need to be derived for these effects for photons since they are different from the ones for the electrons. Simulation data are used to obtain these corrections.

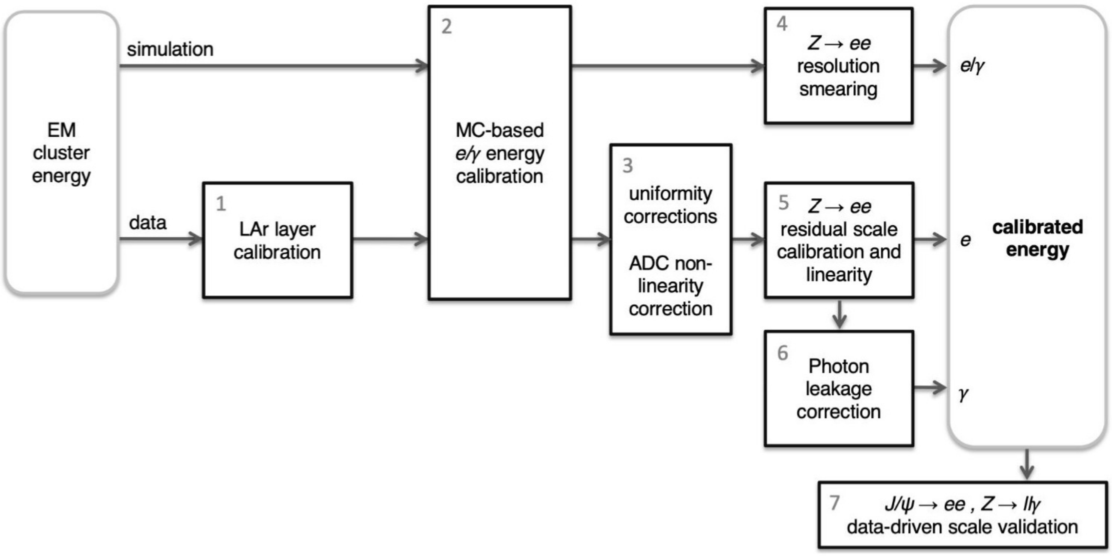

Figure 2: Schematic overview of the electron and photon energy calibration procedure in the ATLAS detector [6].

Validation of the above given calibration procedure is performed using two samples:

- $J/\psi \to ee$ for low energy electron candidates (from 5 to 30 GeV),
- $Z \to ll\gamma$ for photon candidates.

2.4 Determination of the Energy Scale

The energy miscalibration is defined as the difference in response between data and simulation, and is parametrized as follows:

$$E^{DATA} = E^{MC}(1 + \alpha_i) \tag{1}$$

where E^{DATA} and E^{MC} are the electron energies in data and simulation, while α_i represents the departure from optimal calibration, in a given pseudorapidity bin labeled i [1]. In the simulation, the $Z \to ee$ invariant mass peak is centered at the well-known value of the Z mass (91 GeV). Miscalibration in data reflects on the position of this peak, which is shifted from the Z mass. This shift features contributions from both of the electrons that add up to form the invariant mass, which can be represented as:

$$\mu_{ij}^{DATA} = \mu_{ij}^{MC}\sqrt{1 + \alpha_i}\sqrt{1 + \alpha_j}. \tag{2}$$

Here μ^{DATA} and μ^{MC} are the peak positions of the invariant mass distribution for the pair of Z electrons in data and simulation, while α_i and α_j represent the average scale corrections for each of the electrons in the i, j and η bins.

Departure from the optimal Z mass peak position, and by that also the scaling factor α, is not constant for all the energies, i.e. energy correction is not linear. Previous analyses (such as [2]) managed to measure value of the scaling factor for particles with $30 < p_{\mathrm{T}} < 140$ GeV, while the goal of this project is to extend those measurements to the high energy region, above 400 GeV, by finding additional corrections that need to be applied to the electrons located in them. Scaling factors can also vary as a function of pseudorapidity, and this analysis will explore separately corrections for barrel and endcap regions, as well as an inclusive correction.

3 Project Steps Description

The focus of this project is on the particles with higher energies for which the statistics are less abundant, so the first step was to inspect amount of high-energy electron candidates, as well as the kinematics of the available sample. This preliminary analysis of the sample was conducted using the 2018 dataset, to get an overview of possibilities for the next steps. Based on this, a selection of the suitable calibration regions with both high enough energies and statistics was made. Details of this process are provided in Subsections 3.1 and 3.2.

The next step was to perform fits to extract energy scale corrections in the selected regions. Since MC samples with all of the latest calibrations already applied were used, only additional corrections for the high energy electrons needed to be extracted. Several fitting methods were examined, among which a Z-mass line-shape fitting in data and MC proved to be the most adequate for the available sample. The fitting procedure was conducted using the full Run 2 dataset including years 2015, 2016, 2017 and 2018 in order to gain even more statistics enabling a more precise fit. Details of the fitting procedure are provided in Section 3.3.

3.1 Electron selection

For this analysis files from Run 2 Release 22 with matching precision energy calibrations were used.[2] These files are created in a new file format which saves different electron properties for all electrons from an event in form of vectors. No selections were performed on the electrons from the events so they had to be included manually. Events of interest should have passed at least one of the following triggers:

- trigPassed_HLT_e60_lhmedium_nod0
- trigPassed_HLT_e140_lhloose_nod0
- trigPassed_HLT_e300_etcut

The following selections were imposed to isolate the electrons from a $Z \to ee$ decay in the samples:

- only for the MC sample: electron_pass_MatchMC_NOSYS,
- electron_pass_Reconstructed_NOSYS,
- both electrons should pass a medium likelihood selection criterion (electron_pass_Medium_NOSYS),
- the significance of the d0 impact parameter (the transverse impact parameter with respect to the beam line) should be smaller than 5 (electron_absd0sig_NOSYS < 5),
- the distance between the track and the primary vertex should be smaller than 0.5mm in the z plane (electron_pass_z0_NOSYS),
- the number of hits observed in pixel detector should be at least 1 (electron_pixel_hits_n_NOSYS ≥ 1),
- the number of hits observed in silicon detector should be at least 8 (electron_silicon_hits_n_NOSYS ≥ 8),
- the two selected electrons should have opposite electric charge.
- electron invariant mass window from 80 GeV to 100 GeV is considered.

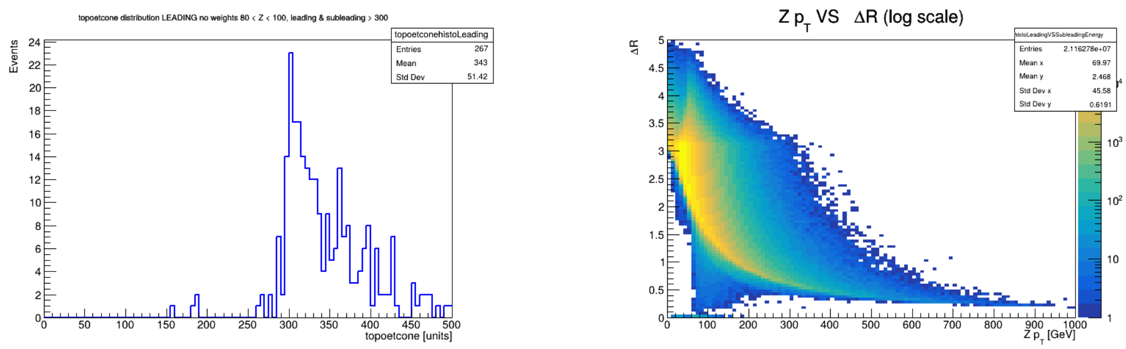

(a) Variable *topoetcone* as function of leading electron's p_{T}.

(b) ΔR as a function of Z p_{T}.

Figure 3: Inspection of the electron isolation.

In order to keep sample statistics as high as possible, no isolation was applied to the electrons, since studies of variables such as *topoetcone40* showed that electrons in the case of boosted Z decay

[2]Files can be found at: "/eos/atlas/atlascerngroupdisk/perf-egamma/egID/electronID/ntuples_tap/v3"

are too close to properly isolate. This is illustrated on Figure 3a, in which said variable has very large values, consistent with the energy of the sub-leading electron in the given event. To further confirm this, a plot of ΔR as a function of the decaying Z p_{T} was also performed, and can be seen on Figure 3b. A rapid decrease in ΔR with growing Z p_{T} indicates that electrons are indeed extremely close in the boosted Z decays.

The aforementioned selections were combined into a single mask vector which was then applied on vectors containing information on electron p_{T}, energy, η, ϕ and charge. Only the events that contained two or more electrons passing the selections were taken into account. Out of the remaining electrons, the two with highest values of p_{T} were selected as leading and sub-leading Z-decay electrons. These electrons were then used in the sample kinematics analysis and finally in the fitting procedures.

3.2 Inspecting kinematics of the sample and available statistics

Since $Z \to ee$ samples are used for the energy calibration, the electron p_T will mostly be in the region around 40 GeV, making the statistics in the lower energy region quite abundant. To examine the amount and kinematics of the high-energy electrons needed for this analysis several plots were performed.

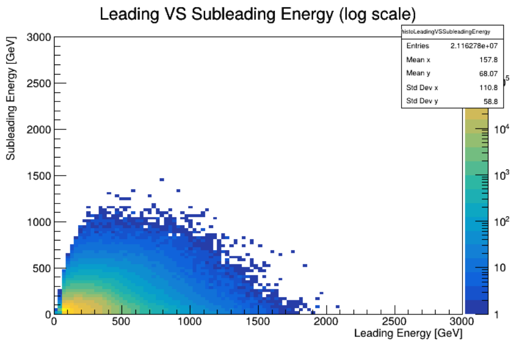

(a) Leading VS Sub-leading electron energy plotted on the log scale.

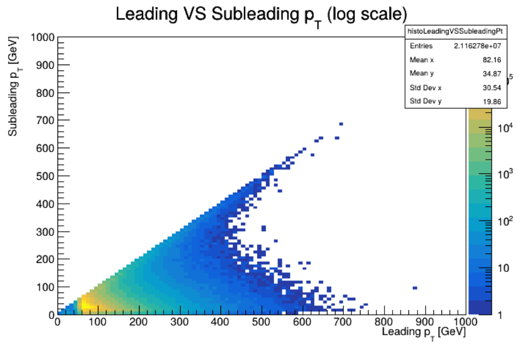

(b) Leading VS Sub-leading electron p_T plotted on the log scale.

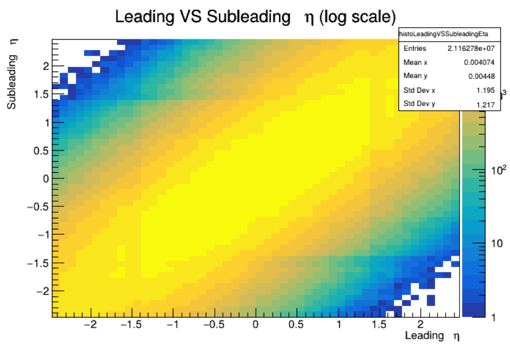

(c) Leading VS Sub-leading electron η plotted on the log scale.

Figure 4: Inspecting MC $Z \to ee$ electron sample kinematics.

Two dimensional histograms of the two electrons energies, p_T and η, presented in Figure 4, were first performed to determine the kinematics of the available MC $Z \to ee$ sample. These plots show that electron energies do not seem to be strongly correlated, but a correlation in η is seen, and as a result of that a partial correlation in p_T, is observed. Correlation of the η is significant since it shows that both electrons have similar η and will therefore mostly be either both in barrel or both in the endcap. On the p_T plot two more dominant regions are observed:

1. asymmetric region along the x-axis - leading electron has high p_{T}, while sub-leading electron has p_{T} in value range around 40 GeV,
2. more symmetric region along the diagonal - both leading and sub-leading electron have high p_{T}, with sub-leading p_{T} still below leading electron p_{T}.

These regions can then be combined in order to acquire even higher statistics.

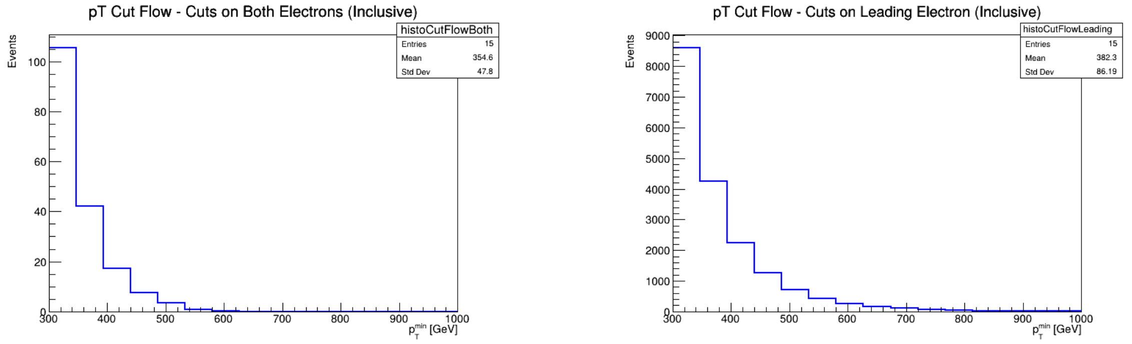

(a) Number of events with energies of both electrons greater than the given value inclusive in η.

(b) Number of events with energies of leading electron greater than the given value inclusive in η.

Figure 5: Comparison of two cut flow plots - much more events are observed when high p_{T} cut is only applied to the leading electron.

Notably not enough events were observed with both of the electrons having high p_{T} of the same order. This was further confirmed by the plots performed to determine the number of electrons present in the dataset with p_T of both electrons above 300 GeV to 1 TeV, exclusively, with steps of 50 GeV. Said plots were performed inclusively in η, and also separately in the barrel ($|\eta| < 1.37$) and in the endcap ($|\eta| > 1.52$). This is illustrated on Figure 5a. Since the fully symmetric events, in which both of the electrons had p_T higher than the given value, were present in the dataset only in smaller numbers, higher p_T cuts were only applied to the leading electron p_T, while less restrictive cuts were applied to the sub-leading electron. One example is given on Figure 5b.

After applying leading electron p_T cuts, $Z \to ee$ invariant mass distributions and corresponding sub-leading p_T distributions were plotted, for the latter looking only at events where the invariant mass of two electrons is in range from 80 to 100 GeV. To determine how well the leading electron can be calibrated in these conditions, the number of events with sub-leading electron p_T in three ranges was calculated:

- **Region 1:** $30 - 50$ GeV, in which sub-leading electron can be assumed to be well calibrated,
- **Region 2:** 50 - cut value GeV, in which additional electron energy correction would need to be applied,
- **Region 3:** greater than cut value, in which high p_{T} correction, main focus of this analysis, is applied to the electrons.

Since low gain depends on the energy and not p_{T}, and since for the same energy but larger η values p_{T} value is lower, cut value will be different for the barrel and endcap region, concretely lower for the endcap region.

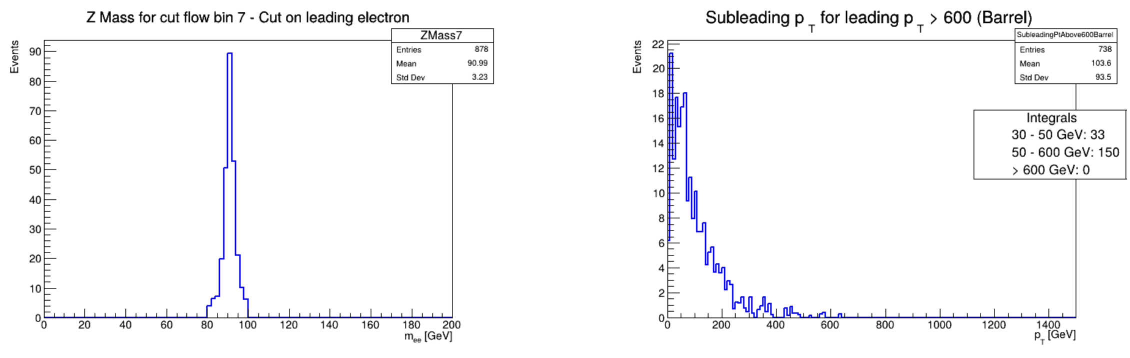

(a) Z-mass peak for leading electron $p_T > 600$.

(b) Sub-leading electron p_T distribution corresponding to 6a.

Figure 6: Example of plots performed for the barrel region.

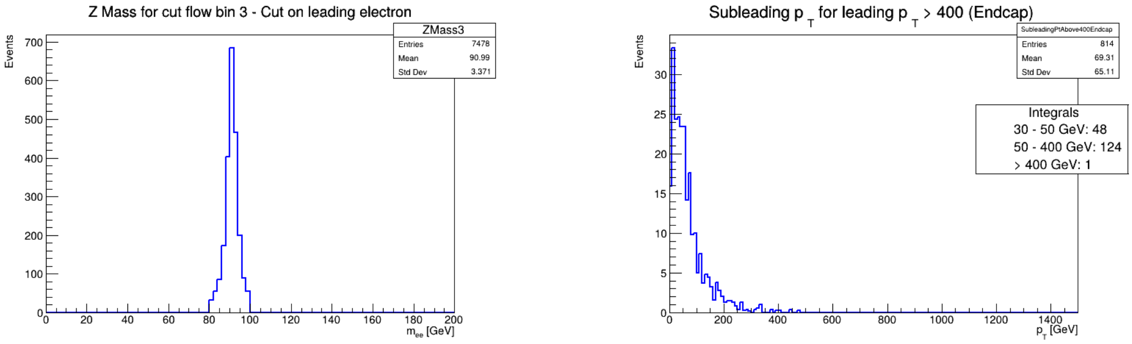

(a) Z-mass peak for leading electron $p_T > 400$.

(b) Sub-leading electron p_T distribution corresponding to 7a.

Figure 7: Example of plots performed for the endcap region.

Examples of plots for the barrel and endcap region can be seen in Figures 6 and 7. The observed results further support the idea of taking into account the very asymmetric Z decays.

Based on this results, it was decided to perform fits in three steps[3], for which details are given in Table 1[4].

Step	**Barrel**	**Endcap**
1	Leading $p_T > 600$ GeV, barrel Sub-leading $30 < p_T < 50$ GeV, inclusive	Leading $p_T > 400$ GeV, endcap Sub-leading $30 < p_T < 50$ GeV, inclusive
2	Leading $50 < p_T < 600$ GeV, barrel Sub-leading $50 < p_T < 600$ GeV, barrel	Leading $50 < p_T < 400$ GeV, endcap Sub-leading $50 < p_T < 400$ GeV, endcap
3	Leading $p_T > 600$ GeV, barrel Sub-leading $p_T > 50$ GeV, barrel	Leading $p_T > 400$ GeV, endcap Sub-leading $p_T > 50$ GeV, endcap

Table 1: Chosen fit regions.

In step 1 the sub-leading electron with p_T from 30 to 50 GeV can be assumed to be well calibrated since it is located in the region with the most abundant statistics from the $Z \to ee$ decays which was studied in previous analysis. In this case a correction α_1 needs to be applied only to the leading electron with high p_T:

$$\mu_{ee}^{DATA} = \mu_{ee}^{MC} \sqrt{(1 + \alpha_1)} \tag{3}$$

Step 2 serves as an intermediate step in which additional corrections α_2 for nonlinearity in the region from 50 GeV to cut value (600 GeV for barrel and 400 GeV for endcap) are derived. It can be divided into three sub-steps, namely from 100 GeV to the cut value, from 75 GeV to 100 GeV and from 50 GeV to 75 GeV, to correct electron energies finer. The correction is in this case same for both of the electrons, as these are symmetric events:

$$\mu_{ee}^{DATA} = \mu_{ee}^{MC}(1 + \alpha_{2i}), \text{ for the } i\text{-th sub-step.} \tag{4}$$

These corrections are then applied to the sub-leading electron in step 3 when its p_T is in one of these ranges. The correction for high-p_T electrons is applied to the leading electron, but also to the sub-leading electron when its p_T is greater than the cut value:

$$\mu_{ee}^{DATA} = \mu_{ee}^{MC} \sqrt{(1 + \alpha_3)} \sqrt{(1 + \alpha_{2i})} \text{ or } \mu_{ee}^{DATA} = \mu_{ee}^{MC}(1 + \alpha_3). \tag{5}$$

[3] Note that steps should not be interpreted as necessarily sequential stages, but rather as distinct components of the fit in which certain logic for finding α correction is applied.

[4] Gap region is excluded so for the case where the sub-leading electron is observed inclusively in η it can be located either in $|\eta| < 1.37$ or in $|\eta| > 1.52$

Step 1 and step 3 should therefore yield the same value for the high-p_T electron correction, i.e., $\alpha_1 \equiv \alpha_3$, meaning that they can either be combined in order to achieve higher statistics, or they can be compared to determine the uncertainty for the correction.

3.3 Performing Fits

Several fitting methods were tested to assess the high-energy electron scale correction, among which:

1. non-simultaneous line-shape fit,
2. simultaneous line-shape fit,
3. template fit.

Unbinned methods were preferred to contain the entire information from the dataset and use it in the fit. Concretely a line-shape fit was used, in which the α correction is extracted directly from the fit, along with corresponding errors, by fitting the invariant mass distribution from MC and data with a known function. A simultaneous version of this fit is used as it has more accurate error propagation for the dependent variables. Description of this method is provided in Subsection 3.3.1. More on the non-simultaneous alternative of this fit can be seen in Appendix A

Template fitting includes comparing Z electron invariant mass distribution in data with the same distribution in MC templates created by inserting different corrections in the nominal MC samples. The value of the correction that yields best compatibility between the data and MC distributions is then chosen. This method requires binning of the dataset, which leads to loss of information that can seriously affect fits of low statistic datasets, as ones present in this analysis. More details can be seen in Subsection 3.3.2.

3.3.1 Line-Shape Fit

In the process of line-shape fitting both MC samples and data were fitted using a convolution of a Breit-Wigner and a Gauss function (called a Voigtian function) in the above-mentioned regions. The width of the Voigtian was fixed to the theoretical value for the width of the Z, which is 2.459 GeV. The σ of the function was allowed to float separately in each fitted region. The mean of this function for the MC sample is extracted from the fit and labeled μ_{ee}^{MC}, while mean of the function for the data sample is μ_{ee}^{DATA} and is expressed as a function of the μ_{ee}^{MC} and α corrections based on the formulas of Equations 3-5.

Step 2 consists, as mentioned before, of three sub-steps with different corrections:

- α_{21} for the electrons with p_{T} from 100 GeV to the cut value,
- α_{22} for the electrons with p_{T} from 75 GeV to 100 GeV,
- α_{23} for the electrons with p_{T} from 50 GeV to 75 GeV.

In steps 1 and 3, the leading electron's p_{T} is always above the cut value, while the sub-leading electron's p_{T} can be in one of the following regions:

- above cut value (Part 0 of Step 3) - correction α_1,
- from 100 GeV to the cut value (Part 1 of Step 3) - correction α_{21},
- from 75 GeV to 100 GeV (Part 2 of Step 3) - correction α_{22},
- from 50 GeV to 75 GeV (Part 3 of Step 3) - correction α_{23},
- from 30 GeV to 50 GeV (Step 1) - no additional correction.

Since all of the parameters are fitted simultaneously, same high energy correction α_1 was used for both Step 1 and Step 3. Even with the full data set it was observed that statistics for Part 0 of Step 3 was extremely low. This region was therefore disregarded in the final fit.

The fit was performed in the following way. First, MC samples were fitted separately (non-simultaneously) for different regions, which enables retrieving the MC mean values. These values are then, along with different α correction variables, used to express correct data means for all of the steps. All data samples are then fitted together in order to simultaneously retrieve all of the α corrections. As a final step, a fully simultaneous version of a fit is performed, in which MC means are again set as free parameters, enabling to also account for their uncertainties when calculating the uncertainties of the α values. Results of the fitting procedure for the barrel and the endcap region can be seen on Figure 8.

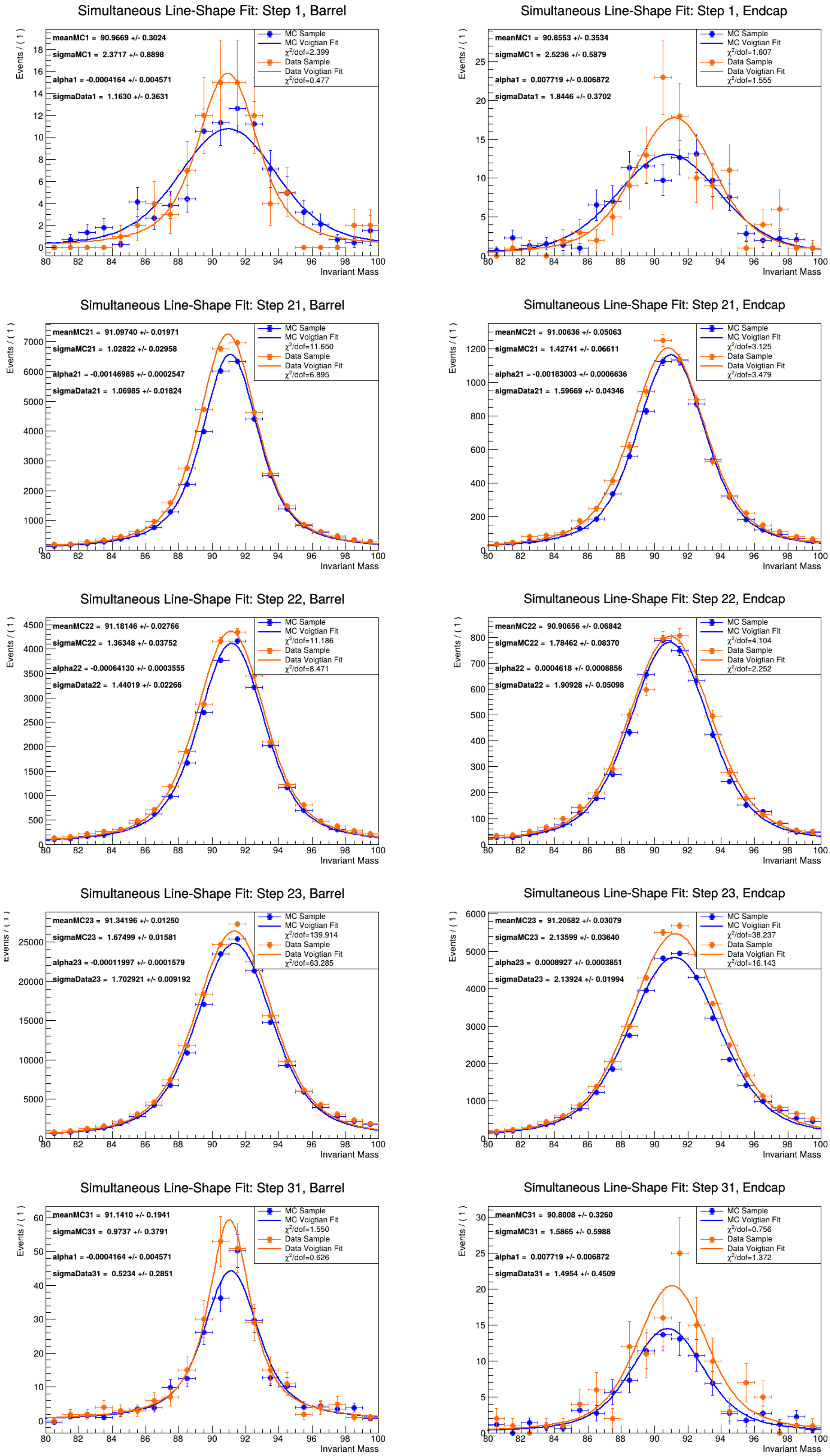

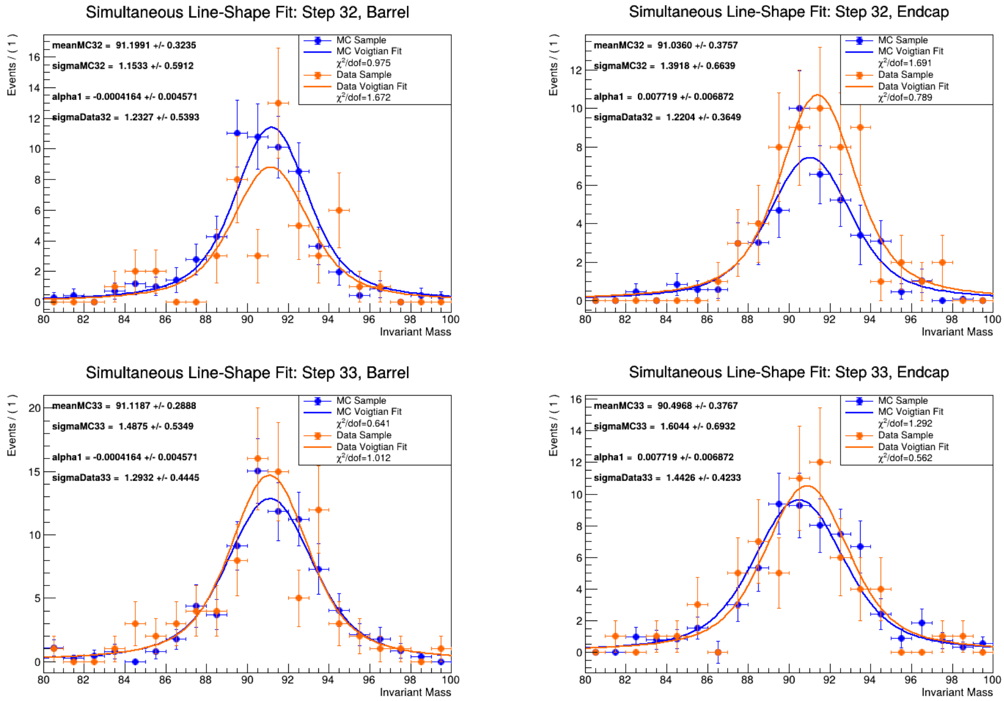

Figure 8: Line-shape fit results for barrel and endcap region.

These results were then combined in order to derive an inclusive correction, which benefits from the higher statistics. Results can be seen on Figure 9.

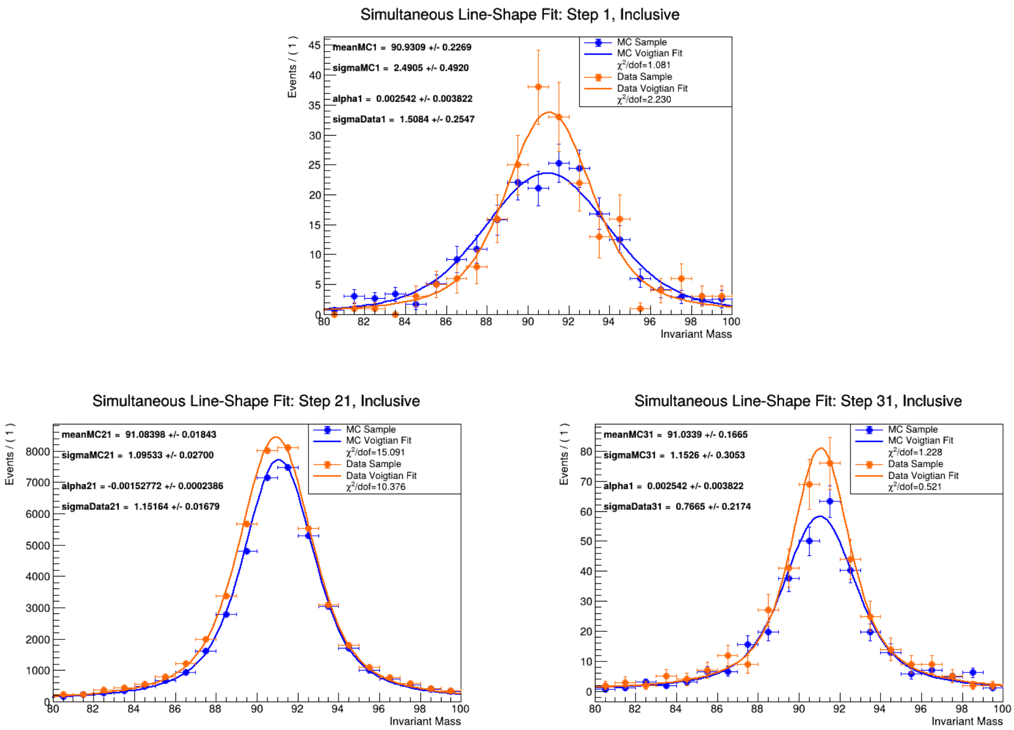

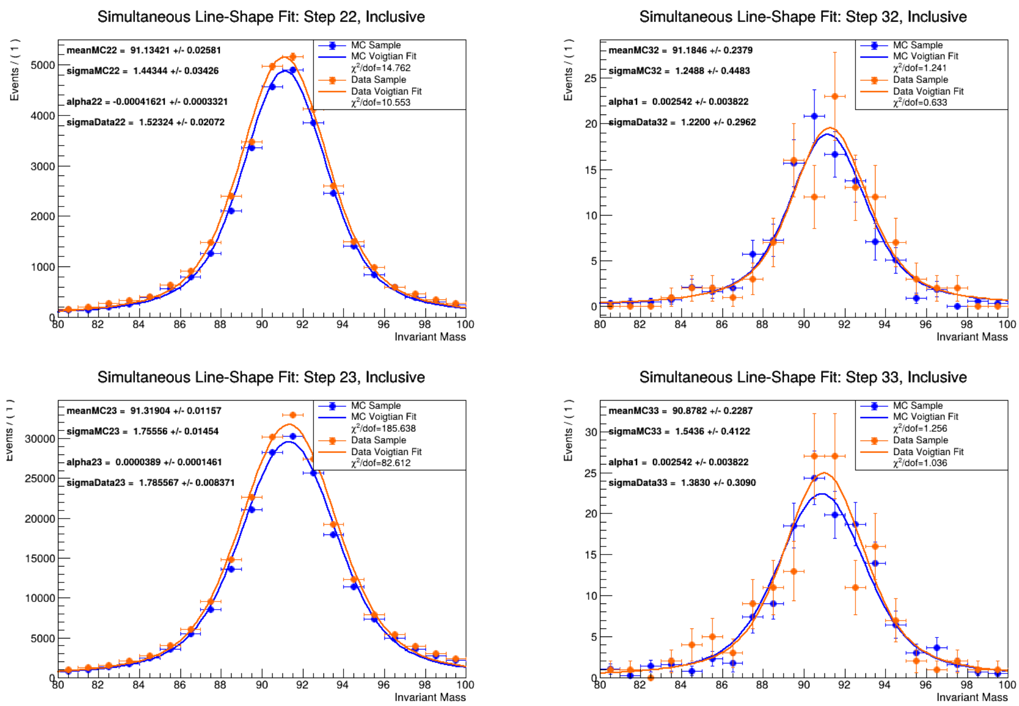

Figure 9: Inclusive line-shape fit results.

During the fitting procedure a difference in MC and data normalization was observed so the missmodeling of Z p_{T} in MC was studied in more detail, but it was discovered that this effect doesn't significantly affect the analysis as it only appears to have an overall normalisation effect but no visible impact on the shape of the Z peak in each fitted region. MC samples were nonetheless reweighted before fitting to better match Data, as can be seen in Appendix B.

3.3.2 Template Fit

Templates for this fit are created by inserting different values of the correction in the nominal MC sample by hand, following the Equations 3-5, and recalculating the invariant mass distribution. In this analysis, α corrections were taken in range from -0.03 to 0.03 with step 0.001. In order to assess the similarity of data and certain template, χ^2 values were calculated for different values of α, and then fitted to a parabola. Minimum of χ^2 parabola represents best value of the α correction. End points of the error interval for this measurement were taken to be values of alpha for which χ^2 value is $min(\chi^2) + 1$.

This procedure was repeated for all of the above-mentioned regions to extract different corrections. Insufficient statistics in combination with the binning required by this method leads to it not being the ideal option. Results shown in Figure 10 are maximally optimized for the low statistics of the sample. Step 1 and 3 are combined into a single step ($\alpha_1 \equiv \alpha_3$) with leading electron's p_{T} above the cut and sub-leading electron's p_{T} above 30 GeV. Additional corrections α_{21}, α_{22}, α_{23} for the sub-leading electron used in this step are derived from the step 2, while the additional high energy correction α_1 is extracted from it.[5] Furthermore, both barrel and endcap regions were combined and large number of bins was used (50 bins for invariant mass window from 80 GeV to 100 GeV).

[5] An additional caveat of this method appears here, namely the error of one correction is not propagated to the other corrections, leading to the smaller final error.

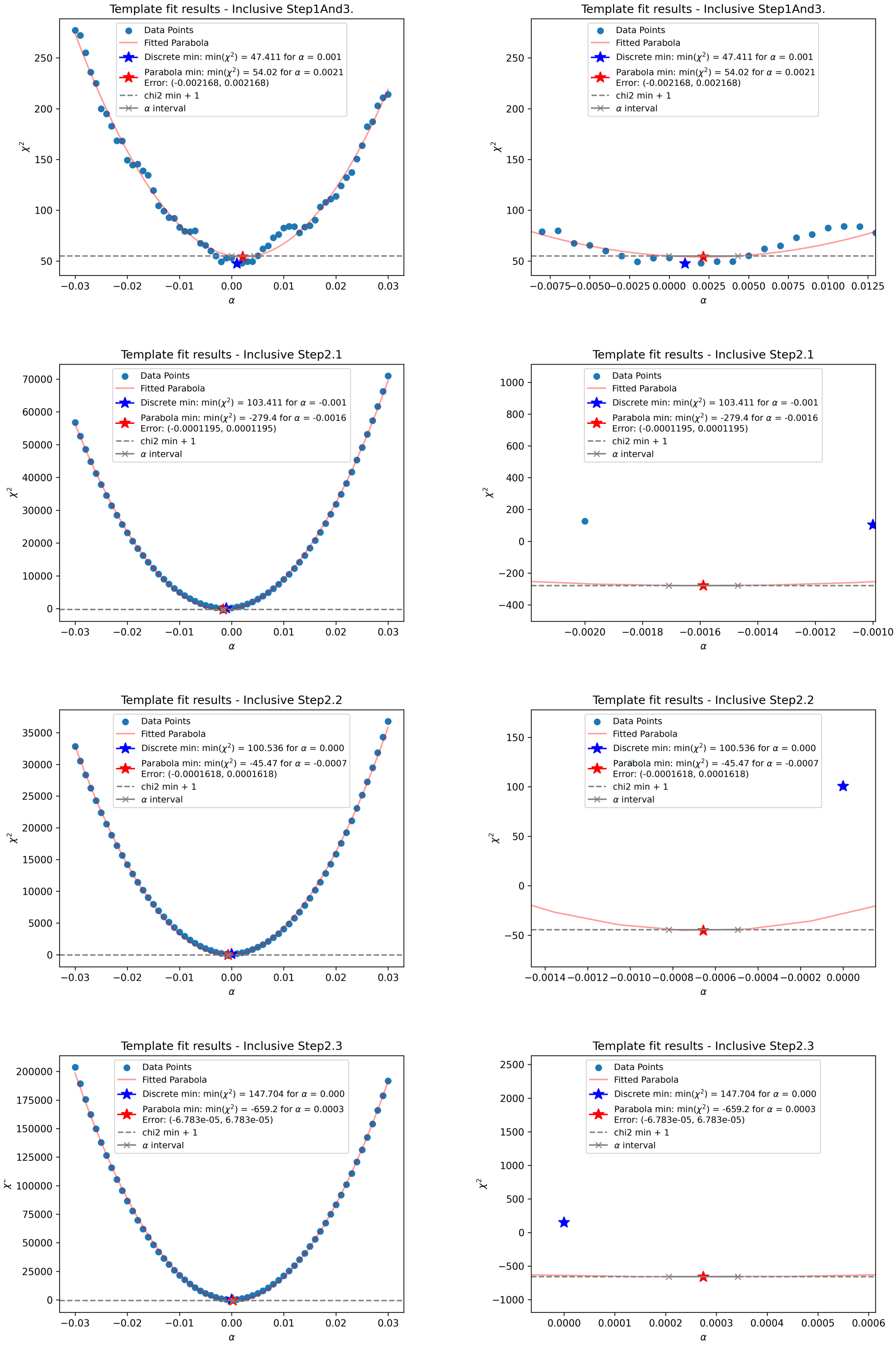

Figure 10: Inclusive template fit results. Plots on the left show zoomed-in region of interest near the parabola minimum.

4 Conclusion

This report describes the first performed measurement of the residual energy scale with high p_T electrons. Results on Figure 11 illustrate values of different α corrections in the barrel (Figure 11a) and endcap region (Figure 11b), as well as the value of inclusive high-energy correction α_1 (Figure 11c), obtained by simultaneous line-shape fit and template fit. Two fitting methods show good overall agreement. However, template fit uncertainties are notably smaller in comparison to the corresponding uncertainty from the line-shape fit. This difference arises from the fact that line-shape fit has much better error propagation mechanism, in which all of the errors for α corrections are correlated, while template fit does not propagate errors of one correction to the others. Uncertainties obtained by the current calibration are also plotted, and it can be seen that they cover potential miscalibrations, but also that, at the moment, statistics are not quite sufficient to reduce this uncertainty. In conclusion, although the presented measurement is severely limited by the statistical uncertainty, no significant deviation from the available calibration was found.

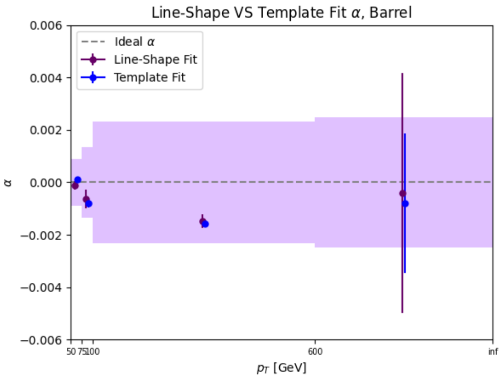

(a)

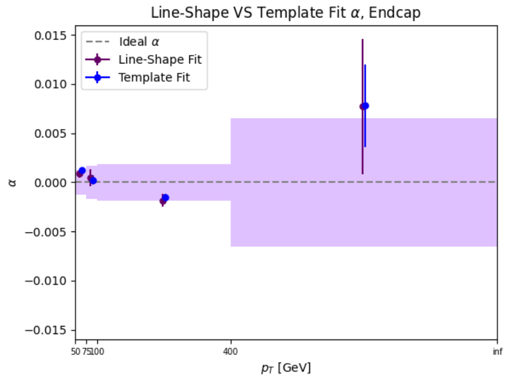

(b)

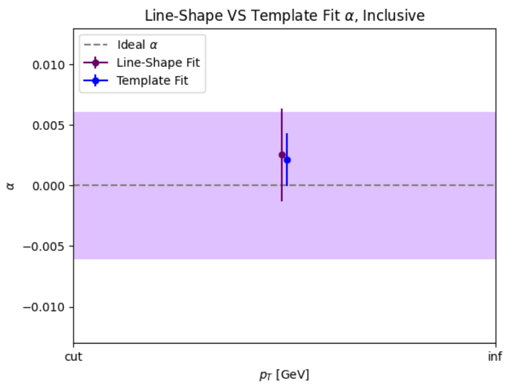

(c)

Figure 11: Comparison of α corrections from line-shape fit and template fit for different fitting regions.

Current project did not include any systematic uncertainties in the measurement. In particular, it would be interesting to examine the effect of electron invariant mass window variation on the values of the correction. All of the fitting procedures reported here were performed in the mass window from 80 GeV to 100 GeV. This and other systematic uncertainty measurements are left for future studies that may benefit from the larger statistics of Run 3.

A Non-Simultaneous Line-Shape Fit

In the non-simultaneous version of the line-shape fit, all of the sub-steps of step 2 are fitted separately, and from each the corresponding corrections α_{21}, α_{22} and α_{23} are derived. Step 1 and 3 can be fitted separately or in combination to derive correction α_1. Due to the low statistics the combination of these steps is preferred. There are then 5 regions of this combined step based on the sub-leading electron p_{T}:

- above cut value,
- from 100 GeV to cut value,
- from 75 GeV to 100 GeV,

- from 50 GeV to 75 GeV,
- from 30 GeV to 50 GeV.

The MC sample is fitted in order to obtain the mean value which is then fixed and used along with the additional constants from step 2 (also as fixed parameters) and the high energy correction α_1 to express the mean of data. A separate PDF is created for each part of the combined step, after which they are summed according to the yield fractions observed in MC to obtain a final PDF for fitting to data. In this procedure α_1 is the only free parameter, and neither errors from other α corrections nor from the MC mean are propagated to its error. The simultaneous line-shape fit is therefore a better choice although the results obtained by this method could be used as an approximation and are seen to be quite consistent with those from the simultaneous fit.

B MC reweighting

Due to the differences in the normalization between MC and data in the various regions studied, mismodeling of the Z p_{T} in MC was studied in more detail. Disagreement between data and MC p_{T} distribution was first studied in four separate η regions relevant for the fitting:

1. both of the electrons in the barrel region ($|\eta| < 1.37$),
2. both of the electrons in the endcap region ($|\eta| > 1.52$),
3. leading electron in the barrel region and sub-leading electron in the endcap region,
4. leading electron in the endcap region and the sub-leading electron in the endcap region.

The result can be seen in Figure 12a. Since all of the inspected regions give similar ratio between data and MC samples, it was decided to use a reweighting inclusive in η, which can be seen on Figure 12*b*.

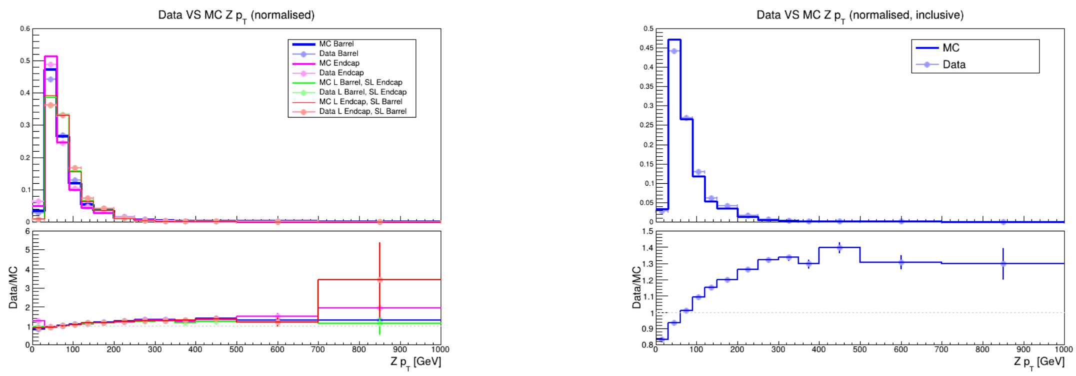

(a) Four different regions based on leading and sub-leading electron η.

(b) Inclusive in η.

Figure 12: Data and MC p_{T} distribution comparison from the 2018 dataset comparison.

Two plots on Figure 13 represent comparison of MC and data line-fit for the 2018 dataset, with (Figure 13a) and without (Figure 13b) reweighting, and illustrate the reweighting effects. It can be noted that only the fit normalization changes, while the fit parameters remain the same, meaning that this effect is of lesser importance for electron energy scale correction derivation.

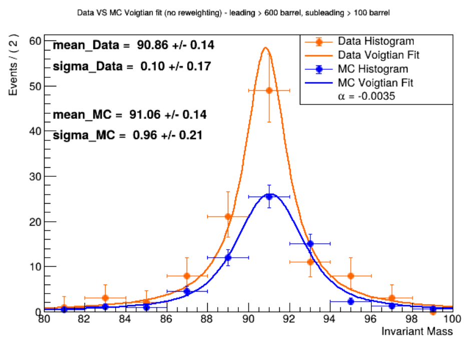

(a) No reweighting applied to the MC sample.

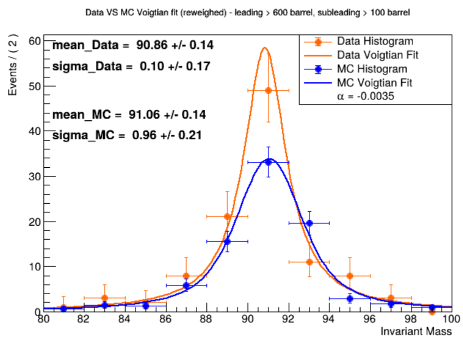

(b) Inclusive reweighting applied to the MC sample.

Figure 13: Effects of reweighting the MC sample illustrated on step 2 of the line-shape fit in the barrel region.

References

[1] ATLAS Colaboration. "Electron and photon energy calibration with the ATLAS detector using LHC Run 1 data". In: *The European Physical Journal C* 74.10 (Oct. 2014). ISSN: 1434-6052. DOI: 10.1140/epjc/s10052-014-3071-4. URL: http://dx.doi.org/10.1140/epjc/s10052-014-3071-4.

[2] ATLAS Colaboration. "Electron and photon energy calibration with the ATLAS detector using LHC Run 2 data". In: *Journal of Instrumentation* 19.02 (Feb. 2024), P02009. ISSN: 1748-0221. DOI: 10.1088/1748-0221/19/02/p02009. URL: http://dx.doi.org/10.1088/1748-0221/19/02/P02009.

[3] ATLAS Collaboration. "The ATLAS Experiment at the CERN Large Hadron Collider". In: *Journal of Instrumentation* 3.08 (Aug. 2008), S08003. DOI: 10.1088/1748-0221/3/08/S08003. URL: https://dx.doi.org/10.1088/1748-0221/3/08/S08003.

[4] Sascha Mehlhase. "ATLAS detector slice (and particle visualisations)". In: *Journal* (2021). URL: https://cds.cern.ch/record/2770815.

[5] ATLAS Colaboration. *ATLAS Open Data - Reconstruction*. Accessed: June 2025. 2025. URL: https://opendata.atlas.cern/docs/documentation/physic_objects/electronphoton_reco.

[6] ATLAS Colaboration. *ATLAS Open Data - Calibrations*. Accessed: June 2025. 2025. URL: https://opendata.atlas.cern/docs/documentation/physic_objects/electronphoton_calibration.